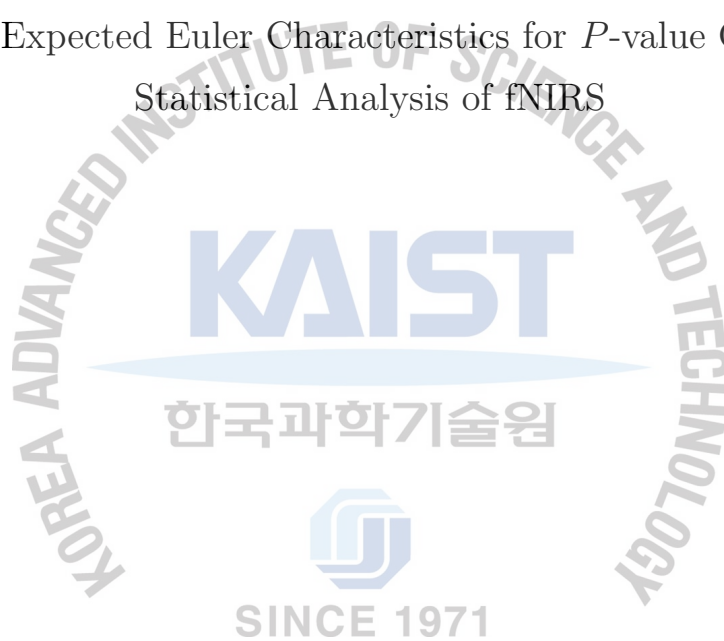


석사 학위논문
Master's Thesis

근적외 분광 뇌활성도 측정 유의도 계산을 위한
LKC-기반 평균 오일러 특성치 분석

LKC-based Expected Euler Characteristics for P -value Correction in
Statistical Analysis of fNIRS



이 화 (李 華 Li, Hua)

바이오및뇌공학과

Department of Bio and Brain Engineering

KAIST

2011

근적외 분광 뇌활성도 측정 유의도 계산을 위한
LKC-기반 평균 오일러 특성치 분석

LKC-based Expected Euler Characteristics for P -value Correction in
Statistical Analysis of fNIRS

KAIST

The logo for KAIST (Korea Advanced Institute of Science and Technology) is centered at the bottom of the page. It consists of the letters 'KAIST' in a bold, blue, sans-serif font. Below the text is a light blue, horizontal, oval-shaped shadow or underline.

LKC-based Expected Euler Characteristics for *P*-value Correction in Statistical Analysis of fNIRS

Advisor : Professor Ye, Jong Chul

by

Li, Hua

Department of Bio and Brain Engineering

KAIST

A thesis submitted to the faculty of KAIST in partial fulfillment of the requirements for the degree of Master of Science in Engineering in the Department of Bio and Brain Engineering. The study was conducted in accordance with Code of Research Ethics¹.

2011. 05. 31.

Approved by

Professor Ye, Jong Chul

[Advisor]

¹Declaration of Ethical Conduct in Research: I, as a graduate student of KAIST, hereby declare that I have not committed any acts that may damage the credibility of my research. These include, but are not limited to: falsification, thesis written by someone else, distortion of research findings or plagiarism. I affirm that my thesis contains honest conclusions based on my own careful research under the guidance of my thesis advisor.

근적외 분광 뇌활성도 측정 유의도 계산을 위한 LKC-기반 평균 오일러 특성치 분석

이 화

위 논문은 한국과학기술원 석사학위논문으로
학위논문심사위원회에서 심사 통과하였음.

The logo for KAIST (Korea Advanced Institute of Science and Technology) is displayed in a light blue color. It consists of the letters 'KAIST' in a bold, sans-serif font, with a horizontal line underneath the letters.

2011년 05월 31일

심사위원장 예 종 철 (인)

심사위원 정 용 (인)

심사위원 남 윤 기 (인)

MBIS
20094313

이 화. Li, Hua. LKC-based Expected Euler Characteristics for P -value Correction in Statistical Analysis of fNIRS. 근적외 분광 뇌활성도 측정 유의도 계산을 위한 LKC-기반 평균 오일러 특성치 분석. Department of Bio and Brain Engineering . 2011. 26p. Advisor Prof. Ye, Jong Chul. Text in English.

ABSTRACT

Functional near-infrared spectroscopy (fNIRS) is a non-invasive imaging approach for measuring brain activities based on changes in the cerebral concentrations of hemoglobin. Recently, statistical analysis based on general linear model (GLM) has become popular. Here, to impose statistical significance on the activation detected by fNIRS, family-wise error (FWE) rate control is important. However, unlike fMRI, where measurements are densely sampled on a regular lattice and Gaussian smoothing makes the resulting random field isotropic, the random fields from fNIRS are non-isotropic due to the interpolation from sparsely and irregularly distributed optode locations. Thus, tube formula based correction has been proposed to address this issue. However, Sun's tube formula is only suitable for Gaussian random field, so it cannot be used for general t - and F - statistics from either individual or group analysis. To overcome these difficulties, we employ the expected Euler characteristic approach based on Lipschitz-Killing curvature (LKC), which has been widely used to address the brain shape analysis. We compared this correction method with Sun's tube formula for individual t random field to confirm the existing method. Based on this comparison, we discovered an important distinction of fNIRS and fMRI such that mass-univariate approach should be modified to consider channel-wise least-square residual correlation. Moreover, by applying this for group level p -value correction, we observe that the ordinary least square estimation is effective for second level analysis due to sensitivity, reduced complexity, and the consistency with individual analysis for the case of precoloring. The new results supplements existing tool of statistical parameter mapping for fNIRS.

Keywords: Near-infrared spectroscopy, statistical parameter mapping, t-test, F-test, family-wise error rate control, expected Euler characteristics, Lipschitz-Killing curvature, mass-univariate approach, mixed-effect analysis

Contents

Abstract	i
Contents	ii
List of Tables	iii
List of Figures	iv
Chapter 1. Introduction	1
Chapter 2. Theory	3
2.1 <i>p</i> -value Correction: EC vs. Tube	3
2.2 Group Analysis for NIRS: OLS vs. GLS	5
Chapter 3. Method	9
3.1 Behavior Protocol	9
3.2 Data Acquisition	9
3.3 Data Analysis	9
Chapter 4. Experimental Results	11
4.1 Individual-level <i>t</i> maps with Tube and expected EC correction	11
4.2 Group-level <i>t</i> maps with OLS-based and GLS-based MFX . . .	13
Chapter 5. Discussion	16
Chapter 6. Conclusion	17
References	24

List of Tables

2.1	Individual-level t - and F - statistics	6
2.2	The comparisons of GLS-based and OLS-based MFX in two approaches	8
4.1	Values of \mathcal{L}_2 with respect to correlation coefficient ρ	12
4.2	Comparison of \mathcal{L}_2 and κ_0 and the corresponding thresholds for Sun's tube formula and LKC-based expected EC with $\rho_2(t)$ (corrected p -value=0.05)	13



List of Figures

2.1	Two schemes of applying contrast: (a) first level approach (Method 1); (b)second level approach (Method 2).	8
4.1	Spatial correlation between least-square residuals at 24 measurement channels in HbO. . .	11
4.2	Individual-level t maps: (a)-(c) Activation maps of HbO, HbR and HbT using Sun's tube formula (corrected p -value $<$ 0.05), and (d)-(f) activation maps of HbO, HbR and HbT using the LKC-based expected EC method (corrected p -value $<$ 0.05).	13
4.3	Group-level t maps using the LKC-based expected EC method: (a)-(c) Activation maps of HbO, HbR and HbT using GLS-based MFX (corrected p -value $<$ 0.1) and the degree of freedom is 6, and (d)-(f) activation maps of HbO, HbR and HbT using OLS-based MFX (corrected p -value $<$ 0.1); the average degree of freedom of HbO is 11, HbR is 12 and HbT is 14.	14
4.4	The ROC curve of GLS and OLS estimations: '□' line represents the ROC curve of OLS with corrected p -value; the '◇' line represents the ROC curve of GLS with corrected p -value.	14
4.5	Group-level F maps using the LKC-based expected EC method: (a) activation map of HbO (corrected p -value $<$ 0.05); (b) activation map of HbR (corrected p -value $<$ 0.05); (c) activation map of HbT (corrected p -value $<$ 0.05).	15

Chapter 1. Introduction

Functional near-infrared spectroscopy (fNIRS) is a non-invasive imaging approach for detecting brain activity via changes in the cerebral concentrations of oxy-hemoglobin (HbO) and deoxy-hemoglobin (HbR) through the “therapeutic optical window” between 650 to 950 nm [25, 4, 7]. Unlike other non-invasive imaging approaches such as functional magnetic resonance imaging (fMRI) and positron emission tomography (PET), fNIRS can directly measure hemodynamic parameters such as HbO, HbR, and total hemoglobin (HbT) at a high temporal resolution under the hypothesis of constant hematocrit. In addition, fNIRS is also very useful to examine the patients and children who might not stand confined environments of fMRI [30]. Moreover, since a fNIRS system is compact, portable and low cost, it has great potential for routine monitoring and many other applications.

Recently, to analyze fNIRS data, statistical analysis based on a general linear model (GLM) becomes popular [30, 16, 12, 29]. Since fNIRS detects the brain activation similar to fMRI, the GLM approach that has been established for fMRI can be applied for fNIRS [30]. More specifically, the GLM expresses the observations in terms of a linear combination of the explanatory variables plus an error term [8]. The explanatory variables constitute the design matrix which encodes and quantifies our knowledge about how the expected signal was produced [8]. The convolution of the stimulation protocol and hemodynamic response function (HRF) is used as a predictor [16]. Moreover, the modeling of latency and dispersion derivatives are also considered as the regressors into the design matrix to compensate for individual and oxygen species specific hemodynamic variation.

There are three main parts in a statistical analysis based on GLM for fMRI and fNIRS: model specification, parameter estimation, and inference [8]. In model specification, the onset time and the duration are necessary to form the experimental paradigm. In order to construct a design matrix, the basis functions should be specified. For parameter estimation, either ordinary least square (OLS) or generalized least square estimations (GLS) is often used. Finally, for inference, a voxel-wise statistical test (i.e., t - or F -tests) constructs the statistical map and then a threshold is determined to detect activation map for a given p -value. Either an uncorrected or a corrected p -value is often applied to determine a threshold. However, an uncorrected p -value only controls the type I error for each voxel independently. Since there are many voxels in the search volume, we are interested to control the type I error for whole search volume. This procedure is termed as family-wise error rate control.

For p -value correction, there are several solutions. If all the voxels in the search volume are independent, Bonferroni correction is very simple and direct method to solve this problem. However, the spatial correlation is very common in functional imaging, so Bonferroni correction often leads to too conservative results [8]. This problem can be addressed by the expected Euler characteristic (EC) method. Euler characteristic is a geometric property of a 3-D volume and can be calculated as the number of connected of the excursion set minus the number of holes plus the number of hollows [31]. When the threshold is high enough, the number of blobs is one or zero. So the expected EC represents the probability of finding an above threshold blob, hence the expected EC is approximately equivalent to the probability of family-wise error [8]. For PET data or smoothed fMRI, it is reasonable to assume that the noise component of image data is isotropic, so the theoretical results for the p -value of local maxima and the size of supra-threshold clusters of a statistical parametric map (SPM) based on random field theory can

be used [27]. However, fNIRS data is non-isotropic, where the full width at half maximum (FWHM) is not same in all directions and across all voxels in the image due to the interpolation from sparsely and irregularly distributed optode locations, so the expected EC method for isotropic random field is not suitable. To address this problem, [29] applied Sun’s tube formula to control the family-wise error rate for individual analysis, since the degree of freedom is large enough to approximate the individual t random field as Gaussian random field. However, in general, Sun’s tube formula is not applicable for statistics such as F at individual and group level because the tube formula is essentially restricted to Gaussian fields [21].

To address the shape analysis in brain imaging, an expression of the excursion probability for general non-isotropic fields on manifolds has been developed by using Lipschitz-Killing curvatures and the kinetic fundamental formulas by warping the random field into a space such that the resulting random fields are isotropic [27]. Here, we term this approach as Lipschitz-Killing curvature (LKC)-based expected EC. LKC is a measure of the intrinsic volume of search volume in the Riemannian metric defined by the variogram [23]. This LKC-based expected EC method can solve the p -value correction problem even for the case of the non-isotropic random field. Hence, the LKC-based expected EC method provides the solution to the family-wise error rate control in fNIRS that has non-isotropic random field due to the inhomogeneous interpolation kernel. Furthermore, one advantage of the Euler characteristic method over the tube formula is that it can be applied to non-Gaussian fields such as t and F random fields. Hence, this formula can be applied for both individual and group analyses.

One of the main contributions of this paper is to verify the accuracy of existing Sun’s tube formula for p -value correction of individual t field. We show that the geometric terms \mathcal{L}_2 in EC and κ_0 in the tube formula are identical for the case of independent channel residuals in fNIRS, but if the channel residuals are correlated, the value of \mathcal{L}_2 is smaller than κ_0 . However, by incorporating channel-wise least-square residual correlation for tube formula, we can verify that the geometric terms \mathcal{L}_2 and κ_0 become identical. The results indicates one important finding that is unique for fNIRS analysis. More specifically, in fMRI, the method of estimating the covariance at each voxel estimates the correlation matrix using restricted maximum likelihood (ReML), and the variance term at each voxel is estimated independently using the usual estimation in a least square mass-univariate scheme [8]. However, in fNIRS, there are only a few measurement channels and the other voxels are interpolated, so the channel-wise least-square residual correlation still exists in variance term estimation, and we need to take into account for this term in calculating the t - and F -statistics. Another contribution of this paper is to show that for a given corrected p -value, mixed-effect analysis by OLS is preferable due to the more sensitivity detection and reduced complexity. Furthermore, when precoloring is used for individual analysis, OLS approach provides more consistent multi-level group analysis. The results in this paper supplement existing statistical analysis in fNIRS by filling the missing components of the toolbox. The new components will be included in the next release of NIRS-SPM which can be downloaded form authors’ homepage. (<http://bisp.kaist.ac.kr/NIRS-SPM.html>)

Chapter 2. Theory

In this section, we will review the LKC-based expected Euler characteristic and discuss individual and the group analyses in NIRS.

2.1 p -value Correction: EC vs. Tube

At a high threshold, the expected EC is approximately equivalent to the probability of a family-wise error [8]. For a non-isotropic random field $Z(r)$ on a manifold Φ , the expected EC φ of excursion set $A_t \equiv A_t(Z, \Phi) = \{r \in \Phi : Z(r) \geq t\}$ at high threshold t is given by [23]:

$$\begin{aligned} P\left(\sup_{r \in \Phi} Z(r) \geq t\right) &\approx E(\varphi(A_t)) \\ &= \sum_{d=0}^D \mathcal{L}_d(\Phi) \rho_d(t), \end{aligned} \quad (2.1)$$

where $\mathcal{L}_d(\Phi)$ is *Lipschitz-Killing curvatures* (LKC) of the manifold Φ representing the intrinsic volume of Φ in a Riemannian metric, and $\rho_d(\cdot)$ denotes the d -dimensional EC density function determined by the type of random fields [23]. For Gaussian random fields, the EC density function is represented by a Hermite polynomial [1], and for general non-Gaussian random fields, the so-called kinetic fundamental formula provides the explicit representation.

For a Gaussian random field $Z(r)$, an excursion probability using the volume of the tube formula is basically the same as Eq. (2.1), except for the zero-th order EC density function $\rho_0(u)$ (See Theorem 10.6.1 in [1]). In particular, the calculation of the LKC can be done explicitly with respect to the basis functions of a finite term Karhunen-Loève expansion [1]. Based on the observation that the t -field can be approximated as a Gaussian random field which possesses a finite Karhunen-Loève expansion, [29] were able to provide a close form expression of the dominant LKC term in the tube formula. However, for general t - and F -statistics in both individual and group analysis, the general LKC-based expected EC formula in Eq. (2.1) is more appropriate and should be exploited.

A method to estimate LKC was developed in [27] and [22], and we review it here briefly. The least-square residual $\mathbf{r}(r) \in \mathbb{R}^N$ of a general linear model is:

$$\mathbf{r}(r) = \mathbf{y}(r) - \mathbf{X}\mathbf{X}^\dagger \mathbf{y}(r), \quad (2.2)$$

where $\mathbf{y}(r) \in \mathbb{R}^N$ are the measurement times series, \mathbf{X} is the design matrix and \dagger is the Moore-Penrose pseudoinverse of a matrix. Then, the corresponding normalized residual is:

$$\mathbf{Q}(r) = \mathbf{r}(r) / \|\mathbf{r}(r)\|_2 \in \mathbb{R}^N.$$

Let

$$\mathbf{S}(r) = (\mathbf{Q}(r + \delta_1) - \mathbf{Q}(r), \dots, \mathbf{Q}(r + \delta_D) - \mathbf{Q}(r)) \in \mathbb{R}^{N \times D}, \quad (2.3)$$

where δ_k is the D -dimensional vector of zeros with k -th component equal to the unit step size along the lattice axis k , $k = 1, \dots, D$. In NIRS topography mapping, the dimension is $D = 2$. (For a tomographic

mapping, $D = 3$). Then, the 2-dimensional LKC of Φ can be estimated as:

$$\hat{\mathcal{L}}_2(\Phi) = \sum_{r \in \Phi} \det(\mathbf{S}(r)' \mathbf{S}(r))^{1/2}, \quad (2.4)$$

where $\det(\cdot)$ denotes the determinant. Estimating the lower dimensional LKC is more complicated, so a short-cut method is often used in practice. Specifically, the D -dimensional LKC, which makes the largest contribution to the p -value approximation, is first estimated. Then, the lower dimensional terms are estimated by simply assuming that Φ is a D -dimensional ball [23]. In NIRS topographic mapping, the dimension is $D = 2$; therefore, we assume that Φ is a disk, and then a short-cut calculation of $\hat{\mathcal{L}}_1(\Phi)$ and $\hat{\mathcal{L}}_0(\Phi)$ can be calculated as:

$$\hat{\mathcal{L}}_0(\Phi) = 1 \quad , \quad \hat{\mathcal{L}}_1(\Phi) = \pi r, \quad (2.5)$$

where $r = \sqrt{\hat{\mathcal{L}}_2(\Phi)/\pi}$. In applying LKC-based expected EC for fNIRS, Eq. (2.3) can be calculated with respect to the interpolation kernel used in NIRS topographic mapping, as shown in Appendix A.

In order to explain tube-based p -value correction, let us first review the individual analysis. Note that the individual-level GLM for the l -th subject at any position $r \in \Phi$ can be written as follows (see Appendix B):

$$\mathbf{y}_l(r) = \mathbf{X} \boldsymbol{\alpha}_l(r) + \boldsymbol{\epsilon}_l(r), \quad (2.6)$$

where $\mathbf{y}_l(r)$ is an N -dimensional time series at the interpolated position $r \in \Phi$, \mathbf{X} is an individual-level design matrix, and $\boldsymbol{\alpha}_l(r)$ is an individual-level response parameter which quantifies the contribution of each regressor, $\boldsymbol{\epsilon}_l(r)$ is a vector representing the error term.

Using the ordinary least square (OLS) approach, we can estimate the individual-level parameter $\hat{\boldsymbol{\alpha}}_l(r)$ and its covariance as:

$$\hat{\boldsymbol{\alpha}}_l(r) = \mathbf{X}^\dagger \mathbf{y}_l(r) \in \mathbb{R}^M \quad , \quad \mathbf{C}_{\hat{\boldsymbol{\alpha}}_l(r)} = \mathbf{X}^\dagger \mathbf{C}_{\boldsymbol{\epsilon}_l(r)} \mathbf{X}^{\dagger T} \in \mathbb{R}^{M \times M}, \quad (2.7)$$

where $\mathbf{C}_{\boldsymbol{\epsilon}_l(r)}$ is the estimation of temporal noise covariance at the interpolated position r . Then, the individual t -statistic can be calculated as follows [29]:

$$T_l(r) = \frac{\hat{\mathcal{X}}_l(r)}{\sqrt{C_{\hat{\mathcal{X}}_l(r)}}}, \quad (2.8)$$

where

$$\hat{\mathcal{X}}_l(r) = \mathbf{c}^T \hat{\boldsymbol{\alpha}}_l(r) = \mathbf{c}^T \mathbf{X}^\dagger \mathbf{y}_l(r) \quad (2.9)$$

$$\begin{aligned} C_{\hat{\mathcal{X}}_l(r)} &= \mathbf{c}^T \mathbf{C}_{\hat{\boldsymbol{\alpha}}_l(r)} \mathbf{c} \\ &= \mathbf{c}^T \mathbf{X}^\dagger \mathbf{C}_{\boldsymbol{\epsilon}_l(r)} \mathbf{X}^{\dagger T} \mathbf{c} \\ &= (\mathbf{b}(r)^T \boldsymbol{\Sigma}_l \mathbf{b}(r)) (\mathbf{c}^T \mathbf{X}^\dagger \boldsymbol{\Lambda}_l \mathbf{X}^{\dagger T} \mathbf{c}), \end{aligned} \quad (2.10)$$

where $\mathbf{b}(r)$ denotes the interpolation kernel, and $\boldsymbol{\Sigma}_l$ is as follows [8, 29]:

$$\boldsymbol{\Sigma}_l = \begin{bmatrix} \sigma_l^{(1)2} & \mathbf{O} & \cdots & \mathbf{O} \\ \mathbf{O} & \sigma_l^{(2)2} & \cdots & \mathbf{O} \\ \vdots & \vdots & \ddots & \vdots \\ \mathbf{O} & \mathbf{O} & \cdots & \sigma_l^{(K)2} \end{bmatrix} \in \mathbb{R}^{K \times K}, \quad (2.11)$$

with variance of each channel:

$$\sigma_l^{(i)2} = \frac{\mathbf{y}_l^{(i)T} \mathbf{R}_X \mathbf{y}_l^{(i)}}{\text{trace}(\mathbf{R}_X \mathbf{\Lambda}_l)}. \quad (2.12)$$

Furthermore, $\mathbf{c} \in \mathbb{R}^M$ denotes the contrast vector and $\mathbf{\Lambda}_l$ is the temporal correlation. The corresponding degree of freedom is:

$$df_l = \frac{\text{trace}(\mathbf{R}_X \mathbf{\Lambda}_l)^2}{\text{trace}(\mathbf{R}_X \mathbf{\Lambda}_l \mathbf{R}_X \mathbf{\Lambda}_l)}, \quad (2.13)$$

where $\mathbf{R}_X = \mathbf{I}_N - \mathbf{X}\mathbf{X}^\dagger$. In our actual experiment, for individual t field, the degree of freedom is around $df_l = 100$ for the case where the number of time points is $N = 5384$ and there are 26677 voxels interpolated from 24 channels.

Due to the large degree of freedom of individual t statistic, it is well-known that t field can be approximated as Gaussian random field, so the tube formula can be applied as follows (for more detail, see [29]):

$$P\left(\sup_{r \in \Phi} Z(r) \geq t\right) \approx \frac{\kappa_0}{2\pi^{\frac{3}{2}}} \Gamma\left(\frac{3}{2}\right) \left(1 - \Gamma\left(\frac{3}{2}, \frac{z^2}{2}\right)\right) \quad (2.14)$$

where

$$\kappa_0 = \sum_{r \in \Phi} \sqrt{|\det(\nabla \mathbf{u}(r)' \nabla \mathbf{u}(r))|} \quad (2.15)$$

$$\mathbf{u}(r) = \frac{\mathbf{C}^{\frac{1}{2}}(\mathbf{b}(r)^T \otimes \mathbf{I}_M) \mathbf{c}}{\sqrt{(\mathbf{b}(r)^T \mathbf{\Sigma} \mathbf{b}(r)) (\mathbf{c}^T \mathbf{X}^\dagger \mathbf{\Lambda} \mathbf{X}^\dagger \mathbf{c})}} \quad (2.16)$$

The formulae of Sun's tube formula (refer to [29]) and LKC-based expected EC methods for 2-dimensional individual t maps are summarized in Table 2.1.

[20] have established that the tube formula and the Euler characteristic method give identical and valid asymptotic expansion of tail probability of the maximum of Gaussian random field when the random field has finite Karhunen-Lo'eve expansion and the index set has positive critical radius [21]. However, this is based on abstract mathematical setting, so we are interested in verifying this using real fNIRS data.

Note that [29] only uses κ_0 term which is the most important constant from Weyl's formula [28]. On the other hand, LKC-based expected EC method includes \mathcal{L}_0 , \mathcal{L}_1 and \mathcal{L}_2 these three terms, where \mathcal{L}_2 has largest contribution. By inspecting the formulae of these two methods, we can find that κ_0 in tube formula corresponds to \mathcal{L}_2 in LKC-based expected EC method. Since the tube formula is restricted to Gaussian fields [21], the other terms $\frac{1}{(2\pi)^{\frac{3}{2}}} z e^{-\frac{z^2}{2}}$ in tube formula corresponds to 2-dimensional EC density of Gaussian random field, whereas LKC-based expected EC method has the 2-dimensional EC density function for t -random field. This implies that there are two sources of differences between tube and EC. One for numerical differences in calculating κ_0 and \mathcal{L}_2 , and the other for the differences in the actual EC density functions. In this paper, we first compare \mathcal{L}_2 and κ_0 to show that the seemingly different two formulae provide the identical results. Then, as the degree of freedom becomes large, the EC density functions for Gaussian and t provide similar threshold values.

2.2 Group Analysis for NIRS: OLS vs. GLS

In neuroimaging applications, a group analysis is very important since researchers are concerned about activation maps in populations of subjects, and analyze data by a multi-subjects approach based

on hypothesis testing at the group level [2]. There are several group analysis methods: one-in-all model, fixed-effects analysis (FFX), random-effects analysis (RFX) and mixed-effects analysis (MFX) [32]. One-in-all model is a straightforward way to carry out group analysis of fMRI data, which formulates a single-level GLM that involves various parameters of interest for the group [6, 13]. However, this method has relatively high human and computational costs [13]. FFX is not sensitive to between-subject variance since the variance of the fixed-effects group mean estimate contains contribution from within-subject variance only. As for RFX, it is not possible to draw pure random effects inferences unless the true GLM parameter vector for single subject is known [3]. MFX includes a mixture of within-subject fixed effects and across-subject random effect, thus generating a so-called mixed effect model. The variance of MFX contains both the within- and between-subject variances. In [8], the RFX refers MFX.

More specifically, the multi-level GLM for group analysis can be formulated as following:

$$\mathbf{Y}(r) = \mathbf{D}\boldsymbol{\alpha}(r) + \boldsymbol{\epsilon}(r), \quad (2.17)$$

$$\hat{\boldsymbol{\alpha}}(r) = \mathbf{X}_{\mathbf{G}}\boldsymbol{\alpha}_{\mathbf{G}}(r) + \boldsymbol{\eta}'(r), \quad (2.18)$$

where $\mathbf{Y}(r)$, $\boldsymbol{\alpha}(r)$ and $\boldsymbol{\epsilon}(r)$ are the stacks of $\mathbf{y}_l(r)$, $\boldsymbol{\alpha}_l(r)$ and $\boldsymbol{\epsilon}_l(r)$ for all L subjects (respectively), $\boldsymbol{\eta}'(r)$ is the group-level error, the first-level design matrix \mathbf{D} is defined as:

$$\mathbf{D} = \mathbf{I}_{L(r)} \otimes \mathbf{X} \in \mathbb{R}^{NL \times ML},$$

and $\boldsymbol{\alpha}_{\mathbf{G}}(r) \in \mathbb{R}^M$ is the group-level vector parameter and the group-level design matrix $\mathbf{X}_{\mathbf{G}}$ is given by:

$$\mathbf{X}_{\mathbf{G}} = \mathbf{1}_L \otimes \mathbf{I}_M = \begin{bmatrix} 1 & 1 & \cdots & 1 \end{bmatrix}^T \otimes \mathbf{I}_M \in \mathbb{R}^{ML \times M}. \quad (2.19)$$

In the second-level GLM, the measurement term $\hat{\boldsymbol{\alpha}}(r)$ obtained by stacking the first level estimated parameters, so MFX makes group-level inferences using the results of separate first-level analyses without having to reanalyze individual subject data.

A MFX based on the GLS approach for both the first and second levels is provided in [2]. [29] used

Table 2.1: Individual-level t - and F - statistics

LKC-based expected EC	Sun's tube formula
$P(\sup_{r \in \Phi} Z(r) \geq t)$ $\approx \sum_{d=0}^D \mathcal{L}_d(\Phi) \rho_d(t)$	$P(\sup_{r \in \Phi} Z(r) \geq t)$ $\approx \frac{\kappa_0}{2\pi^{\frac{3}{2}}} \Gamma\left(\frac{3}{2}\right) \left(1 - \Gamma\left(\frac{3}{2}, \frac{z^2}{2}\right)\right)$ $\sim \kappa_0 \frac{1}{2\pi^{\frac{3}{2}}} z e^{-\frac{z^2}{2}}$
$\mathcal{L}_2(\Phi) = \sum_{r \in \Phi} \sqrt{ \det(\nabla \mathbf{Q}_l(r)' \nabla \mathbf{Q}_l(r)) }$	$\kappa_0 = \sum_{r \in \Phi} \sqrt{ \det(\nabla \mathbf{u}(r)' \nabla \mathbf{u}(r)) }$
$\mathbf{Q}_l(r) = \frac{\mathbf{r}(r)}{\ \mathbf{r}(r)\ }$	$\mathbf{u}(r) = \frac{\mathbf{c}^{\frac{1}{2}} (\mathbf{b}(r)^T \otimes \mathbf{I}_M) \mathbf{c}}{\sqrt{(\mathbf{b}(r)^T \boldsymbol{\Sigma} \mathbf{b}(r)) (\mathbf{c}^T \boldsymbol{\Lambda} \mathbf{c})}}$
$\rho_2(t) = \frac{1}{2\pi^{\frac{3}{2}}} \frac{\Gamma\left(\frac{v+1}{2}\right)}{\left(\frac{v}{2}\right)^{\frac{1}{2}} \Gamma\left(\frac{v}{2}\right)} \left(1 + \frac{t^2}{v}\right)^{-\frac{v-1}{2}}$	$\rho_2(z) = \frac{1}{2\pi^{\frac{3}{2}}} z e^{-\frac{z^2}{2}}$

this framework to derive the specific formula for fNIRS which is applied in NIRS-SPM:

$$T_G(r) = \frac{\sum_{l=1}^L \frac{\hat{\chi}_l(r)}{C_{\hat{\chi}_l(r)} + \sigma_s^2(r)}}{\sqrt{\sum_{l=1}^L \frac{1}{C_{\hat{\chi}_l(r)} + \sigma_s^2(r)}}}, \quad (2.20)$$

where σ_s^2 is the between-subject variance, $\hat{\chi}_l(r)$ and $C_{\hat{\chi}_l(r)}$ denote the l -th individual-level parameter specified by a contrast vector \mathbf{c} and its within-subject variance (for more details, please refer to [29]). Due to the whitening operation in the group level, the degree of freedom for the group t -map from GLS is equal to the number of subjects minus one. Hence, if the number of subjects is not sufficient, the degree of freedom is not large enough. Therefore, Gaussian approximation of t -field is not accurate for the group analysis, when the number of subjects is not large, so tube formula cannot be used. In addition, in order to match the individual and group analyses, both of the analyses should be done using generalized least square estimation. This implies the prewhitening process is requested at individual level, and precoloring often results in sub-optimal estimation. The main problem of prewhitening in fNIRS analysis is that due to the length of the time series, the memory and computational costs are very expensive. Furthermore, it was shown that precoloring is often more preferable for individual analysis in fNIRS [29]. Therefore, in this paper the OLS-based MFX is derived to make the group-level analysis consistent with the individual analysis in NIRS-SPM with precoloring. The detailed derivation is shown in Appendix C. More specifically, the group-level t -statistic in OLS-based MFX can be formed as follows:

$$T_G(r) = \frac{\mathbf{c}^T \hat{\boldsymbol{\alpha}}_G(r)}{\sqrt{\mathbf{c}^T \mathbf{C}_{\hat{\boldsymbol{\alpha}}_G(r)} \mathbf{c}}}, \quad (2.21)$$

where $\hat{\boldsymbol{\alpha}}_G(r)$ and $\mathbf{C}_{\hat{\boldsymbol{\alpha}}_G(r)}$ are estimated group-level parameter and its covariance can be represented using Eq. (2.9):

$$\begin{aligned} \hat{\boldsymbol{\alpha}}_G(r) &= \frac{1}{L} \sum_{l=1}^L \hat{\boldsymbol{\alpha}}_l(r), \\ \mathbf{C}_{\hat{\boldsymbol{\alpha}}_G(r)} &= \frac{1}{L^2} \sum_{l=1}^L (\sigma_s^2 \mathbf{I}_M + \mathbf{C}_{\hat{\boldsymbol{\alpha}}_l(r)}). \end{aligned}$$

The corresponding degree of freedom is given by [17, 26]:

$$df_G = \frac{\sum_{l=1}^L (\sigma_s^2 + C_{\hat{\chi}_l(r)})^2}{\frac{L^2 \sigma_s^4}{L-1} + \sum_{l=1}^L \frac{C_{\hat{\chi}_l(r)}^2}{df_l}},$$

where df_l is the degree of freedom of the individual-level t -statistic.

Another advantage of OLS comes from applying contrast vector. More specifically, as for carrying out MFX, both NIRS-SPM and SPM apply contrast vector (for example, $\mathbf{c} = [1 \ 0 \ 0 \ 0]$) at individual level for each subject, and put the contrasts of estimated individual parameters $\hat{\chi}_l(r) = \mathbf{c}^T \hat{\boldsymbol{\alpha}}_l(r)$ into second-level GLM of MFX (see Fig. 2.1(a)). This ensures that there is only one observation per subject in the second-level analysis and the group-level parameter $\hat{\chi}_G(r)$ is estimated directly. However, there exist disadvantages in this approach. If we want to change the contrast vector (for example, to change $\mathbf{c} = [1 \ 0 \ 0 \ 0]$ to $\mathbf{c} = [1 \ 1 \ 1 \ 0]$), we should reanalyze all the individual data since the contrast vector has been already applied at individual level. Instead of applying contrasts at individual level as $\hat{\chi}_l(r) = \mathbf{c}^T \hat{\boldsymbol{\alpha}}_l(r)$, we want to transfer the estimated individual parameters without applying contrast vector $\hat{\boldsymbol{\alpha}}_l(r)$ into

second-level GLM and then obtain the estimated group-level vector parameter $\hat{\alpha}_G(r)$. Then, we may apply the contrast vector to obtain $\hat{\chi}_G(r) = \mathbf{c}^T \hat{\alpha}_G(r)$ (see Fig. 2.1(b)). In this case, we can change the contrast vector at group level directly without reanalyzing all individual data. One of the advantages of

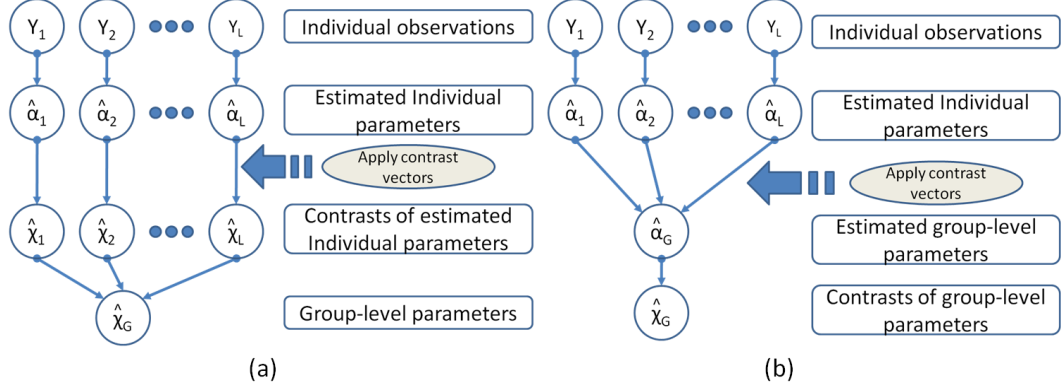


Figure 2.1: Two schemes of applying contrast: (a) first level approach (Method 1); (b) second level approach (Method 2).

OLS-based group analysis is that the two approaches provides equivalent results, which is not the case of GLS as shown in Table 2.2.

The group-level F -statistic can be also easily formed as follows [8]:

$$F_G(r) = \frac{\hat{\alpha}(r)^T (\mathbf{R}_{X_{G_0}} - \mathbf{R}_{X_G}) \hat{\alpha}(r) / \text{trace}(\mathbf{R}_{X_{G_0}} - \mathbf{R}_{X_G})}{\hat{\alpha}(r)^T \mathbf{R}_{X_G} \hat{\alpha}(r) / \text{trace}(\mathbf{R}_{X_G})} \quad (2.22)$$

where $\mathbf{R}_{X_G} = \mathbf{I} - \mathbf{X}_G \mathbf{X}_G^\dagger$ and $\mathbf{R}_{X_{G_0}} = \mathbf{I} - \mathbf{X}_{G_0} \mathbf{X}_{G_0}^\dagger$ from which $\mathbf{X}_{G_0} = \mathbf{X}_G (\mathbf{I} - \mathbf{C} \mathbf{C}^\dagger)$ is the reduced design matrix. The corresponding degrees of freedom are:

$$\begin{aligned} df_{G_1} &= \text{trace}(\mathbf{R}_{X_{G_0}} - \mathbf{R}_{X_G}), \\ df_{G_2} &= \text{trace}(\mathbf{R}_{X_G}). \end{aligned}$$

Table 2.2: The comparisons of GLS-based and OLS-based MFX in two approaches

	GLS based MFX	OLS based MFX
Method 1	$\hat{\chi}_G(r) = \frac{\sum_{l=1}^L \frac{\hat{x}_l(r)}{c \hat{x}_l(r) + \sigma_s^2(r)}}{\sum_{l=1}^L \frac{1}{c \hat{x}_l(r) + \sigma_s^2(r)}}$	$\hat{\chi}_G(r) = \frac{1}{L} \sum_{l=1}^L \hat{x}_l(r)$
	⋈	⋈
Method 2	$\hat{\chi}_G(r) = \mathbf{c}^T \hat{\alpha}_G(r)$ $= \mathbf{c}^T (\mathbf{X}_G^T \mathbf{C}_{\eta'}^{-1} \mathbf{X}_G)^{-1} \mathbf{X}_G^T \mathbf{C}_{\eta'}^{-1} \hat{\alpha}(r)$	$\hat{\chi}_G(r) = \mathbf{c}^T \hat{\alpha}_G(r)$ $= \frac{1}{L} \sum_{l=1}^L \hat{x}_l(r)$

Chapter 3. Method

3.1 Behavior Protocol

Right finger tapping (RFT) experiments were chosen to verify the validity of the proposed method. The number of subjects was seven. The data were published by [29] and the entire recording time was 552 seconds. The experimental paradigm was composed of 21-second tapping and 30-second rest for each subject, which was repeated 10 times. All subjects were right-handed and all had no history of neurological disease. Participants were given instructions regarding the experimental process of the NIRS and MRI, and all provided written informed consent. This study was approved by the Institutional Review Board of the Korea Advanced Institute of Science and Technology (KAIST).

3.2 Data Acquisition

An NIRS instrument (Oxyton MK III, Artinis, Netherlands) with 24 channels, 8 sources, and 4 detectors was used to measure the optical density variation at two wavelengths of 781 nm and 856 nm at a sampling frequency of 10 Hz. A holder cap to fix the distance between the optodes was attached to the scalp around the primary motor cortex. The distance between the source and the detector was 3.5 cm. To ensure an accurate anatomical scanning session, T1-weighted structural images were acquired using a 3.0 T MRI system (ISOL, Republic of Korea). After the data were acquired, we converted the optical densities to concentration changes of oxy- and deoxy-hemoglobin. We applied wavelet-MDL detrending [10] to remove the global drift, since this approach provides more consistent and reliable detrending results. Finally, the individual and group analyses were performed as discussed in Section 2.

3.3 Data Analysis

For individual analysis, we use NIRS-SPM toolbox to construct the individual t maps and use the Sun's tube formula to do the p -value correction. We also control the family-wise error rate with LKC-based expected EC and compare its result with that of tube formula. For group analysis, we use NIRS-SPM to construct group-level t random field, in which the GLS-based MFX is used. At the same time, we also apply the OLS-based MFX and compare its result with that of GLS-based MFX using ROC analysis.

In signal detection theory, a receiver operating characteristic (ROC) space is defined by false positive rate (FPR) and true positive rate (TPR) as x and y axes (respectively), thereby depicting the relative trade-off between true positive rate (TPR) and false positive rate (FPR):

$$\begin{aligned} TPR &= \frac{TP}{P}, \\ FPR &= \frac{FP}{N}, \end{aligned}$$

where P is positive, N is negative, TP is true positive, and FP is false positive, respectively. Each prediction result represents one point in the ROC space. In the statistical detection of activation in

NIRS, this paper chooses a simultaneously recorded fMRI image (uncorrected $p < 0.001$) as ground truth and applies the ROC curve to judge the activation of NIRS. In this case, the true positive (TP) is the area where activations of fMRI and NIRS overlap; the false positive (FP) is the area which shows the activation in NIRS but not in fMRI; the false negative is the area which shows activation in fMRI but not in NIRS; and the true negative is the area where inactivations of fMRI and NIRS overlap. Therefore, the sensitivity refers to how much the area where activations of fMRI and NIRS overlap takes up within the overall area of ground truth. Hence, a low sensitivity value does not necessarily mean that most of the activations in NIRS were outside of the ground truth; such values could be due to a small activation area. High specificity means that very few voxels of activation in NIRS were outside of the ground truth.



Chapter 4. Experimental Results

4.1 Individual-level t maps with Tube and expected EC correction

To compare the tube formula and EC method, first we use simulation data to compare κ_0 and \mathcal{L}_2 . We construct random Gaussian residuals of length of $N = 5384$ with the variances equal to the real residual of HbO for each channel, and then calculate κ_0 and \mathcal{L}_2 , respectively. Recall that the channel-wise least-square residual time series refer Eq. (2.2), which corresponds to the time series after projecting the measurements to the null-space of design matrix. In calculating κ_0 and \mathcal{L}_2 , we use the same interpolation kernel as in real data assuming the equivalent imaging geometry. The results show that $\kappa_0 = 50.5381$ and $\mathcal{L}_2 = 50.8717$, which are nearly identical. However, when we use real HbO time series, we find that $\mathcal{L}_2 = 19.8468$, whereas κ_0 remains same. To explore the main causes to make \mathcal{L}_2 decrease, we first consider the temporal correlation Λ_t . We add temporal correlation to the simulation data by smoothing and then calculate \mathcal{L}_2 again. However, the result is $\mathcal{L}_2 = 52.4097$. Hence, temporal correlation was not the cause. Next we consider the spatial correlation. Fig. 4.1 shows the channel-wise spatial correlation structures of channel-wise least-square residual from real measurements. We can find that real data has spatial correlation between different channels. Unlike the mass-univariate assumption in SPM or NIRS-SPM where each voxel has independent variance, it turns out that the least-square residuals from different fNIRS channels are still quite correlated, maybe due to global trend or remaining activation patterns that cannot be removed by projecting to null space of design matrix. To verify that spatial correlation is the main cause, we added spatial correlations to the simulation data using AR(1) process across channels with parameter ρ . Table 4.1 summarizes the values of \mathcal{L}_2 for various ρ 's. We find that \mathcal{L}_2 decreases as the spatial correlation increases.

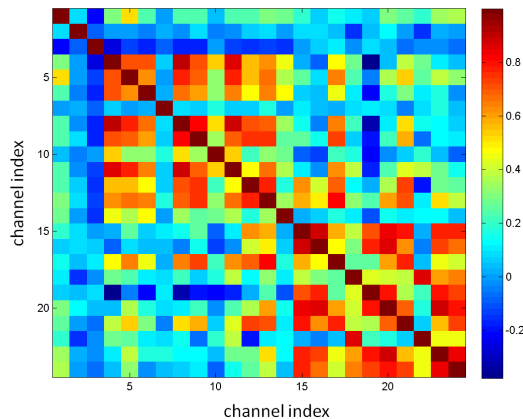


Figure 4.1: Spatial correlation between least-square residuals at 24 measurement channels in HbO.

Recall that the mass-univariate assumption in SPM and NIRS-SPM state that there is no spatial correlation between different channel noises even though the temporal correlation matrix is estimated across voxels by pulling [8]. Hence, a diagonal matrix Σ_t was shown in Eq. (2.11). However, since there

exists significant spatial correlation in real residual data, we may abandon the assumption that $\mathbf{\Sigma}_l$ is a diagonal matrix. Instead, the (i, j) -th element of the $\mathbf{\Sigma}_l$ is now calculated by

$$\sigma_l^{(ij)2} = \frac{\mathbf{y}_l^{(i)T} \mathbf{R}_X \mathbf{y}_l^{(j)}}{\text{trace}(\mathbf{R}_X \mathbf{\Lambda}_l)}, \quad (4.1)$$

to incorporate the correlation structure. Using this correlation, the result of tube formula yields $\kappa_0 = 19.8393$, which is basically same as $\mathcal{L}_2 = 19.8468$. This indicates that whatever the reason for the spatial correlation in the least-square residuals, we should include it to make the tube formula more accurate. Furthermore, in calculating Eq. (2.10), we should include the non-diagonal form of $\mathbf{\Sigma}_l$ by using Eq. (4.1). The effect is that overall t -values are reduced. Therefore, in the following experiments, we modified NIRS-SPM to reflect this observation.

Next, we compare the thresholds produced by these two methods. The goal is to check the accuracy of Sun’s tube formula which is based on approximating individual t random field as Gaussian random field. Since only κ_0 term is used in Sun’s tube formula, only \mathcal{L}_2 is included in LKC-based expected EC method for a fair comparison.

For expected EC method, the EC density of t random field $\rho_2(t)$ is used, whereas the tube formula uses the EC density function of Gaussian random field. Table 4.2 shows the thresholds for HbO, HbR and HbT. As discussed before, the κ_0 and \mathcal{L}_2 are nearly identical, so the difference in threshold mainly comes from different EC density functions. As expected by theory, the threshold of LKC-based expected EC is a little larger than that of Sun’s tube formula due to the difference in t and Gaussian field. However, the threshold difference is so small that the activation maps produced by these two methods are similar as shown in Fig. 4.2. Note that for both two correction methods, the activation maps are all around the primary motor cortex. More specifically, Figs. 4.2 (a)-(c) show the activation maps of HbO, HbR, and HbT, with p -values corrected by Sun’s tube formula (corrected $p < 0.05$). Figs. 4.2 (d)-(f) show the activation maps of HbO, HbR and HbT corrected by the LKC-based expected EC (corrected $p < 0.05$). In the right finger tapping task, the main target area is the primary motor cortex (BA 4). The equivalence between tube and EC are consistently observed for other individual data (results are not shown).

Table 4.1: Values of \mathcal{L}_2 with respect to correlation coefficient ρ

ρ	\mathcal{L}_2
0	50.8717
0.1	50.0378
0.2	48.9988
0.3	47.4781
0.4	45.1554
0.5	41.6781
0.6	36.7028
0.7	30.0050
0.8	21.7198
0.9	12.7779

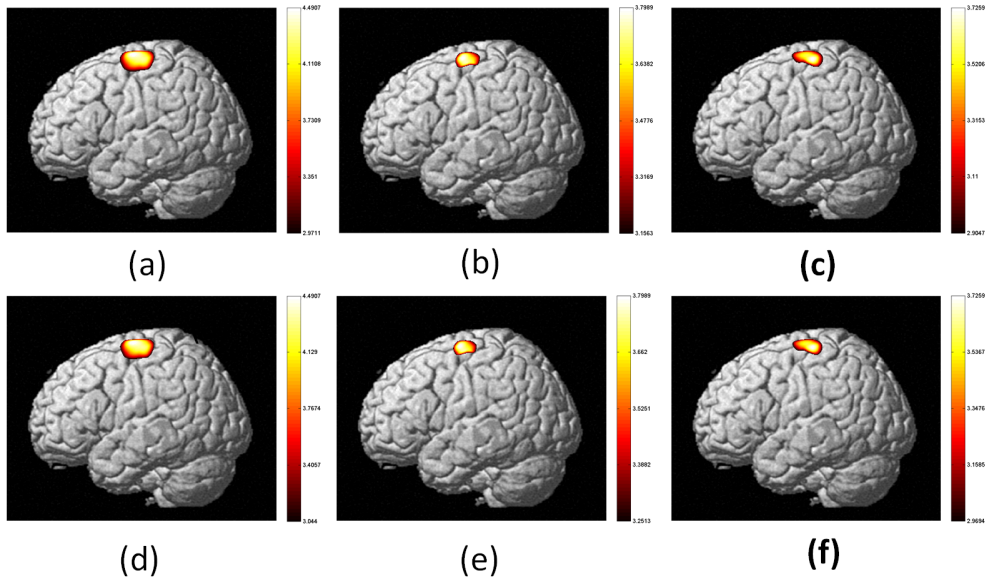


Figure 4.2: Individual-level t maps: (a)-(c) Activation maps of HbO, HbR and HbT using Sun's tube formula (corrected p -value < 0.05), and (d)-(f) activation maps of HbO, HbR and HbT using the LKC-based expected EC method (corrected p -value < 0.05).

4.2 Group-level t maps with OLS-based and GLS-based MFX

In this paper, the group-level t maps are constructed using OLS-based MFX in order to be consistent with the individual analysis using precoloring. At the same time, the group-level t maps are also constructed using NIRS-SPM where GLS-based MFX is used. Figs. 4.3(a)-(c) show the activation maps from the t -test for HbO, HbR and HbT by GLS-based MFX, whereas (d)-(f) are those by OLS-based MFX. The number of subjects is 7, and the corrected p -value is set a little bit high to $p < 0.1$ to compensate the small number of subjects. The p -value correlation was based on expected Euler characteristics using LKC formula.

All the activation maps of HbO and HbT are around the primary motor cortex. However, compared to the activation area of HbO and HbT using OLS-based MFX, the activation maps of HbO and HbT with GLS-based MFX are relatively conservative. There is no significant activation in HbR for GLS-based MFX, while there exists significant activation in HbR for OLS-based MFX. This indicates that OLS-based MFX is more sensitive.

The result in Fig. 4.3 illustrates that for the same corrected p -value, the activation area of OLS is larger than that of GLS. To study this further, we carry out the ROC analysis. Fig. 4.4 shows the

Table 4.2: Comparison of \mathcal{L}_2 and κ_0 and the corresponding thresholds for Sun's tube formula and LKC-based expected EC with $\rho_2(t)$ (corrected p -value=0.05)

	κ_0	\mathcal{L}_2	threshold-tube	threshold-EC	Difference
HbO	19.8393	19.8468	2.9710	3.0440	0.0730
HbR	33.0227	33.0266	3.1540	3.2510	0.0970
HbT	16.5739	16.6013	2.9040	2.9680	0.0640

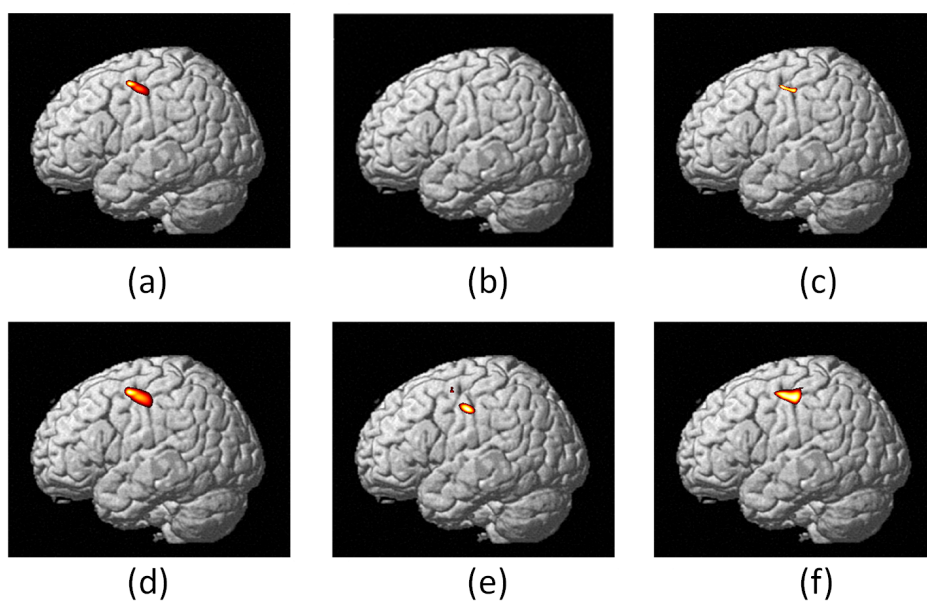


Figure 4.3: Group-level t maps using the LKC-based expected EC method: (a)-(c) Activation maps of HbO, HbR and HbT using GLS-based MFX (corrected p -value < 0.1) and the degree of freedom is 6, and (d)-(f) activation maps of HbO, HbR and HbT using OLS-based MFX (corrected p -value < 0.1); the average degree of freedom of HbO is 11, HbR is 12 and HbT is 14.

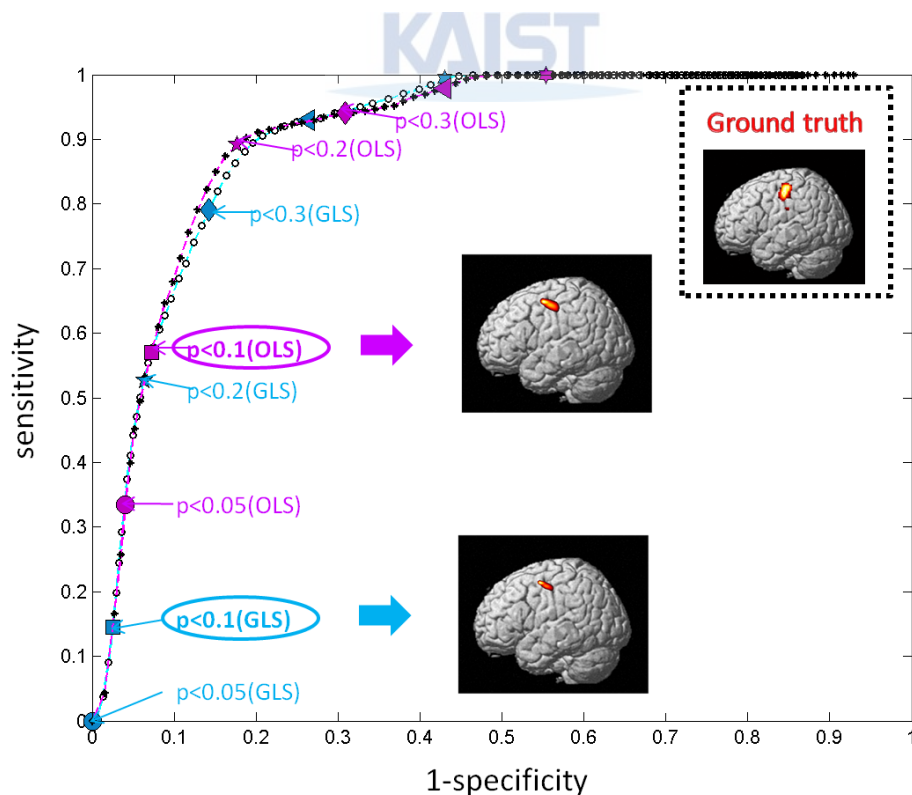


Figure 4.4: The ROC curve of GLS and OLS estimations: '□' line represents the ROC curve of OLS with corrected p -value; the '◇' line represents the ROC curve of GLS with corrected p -value.

ROC curves of GLS and OLS estimations. Here, the ground-truth image was obtained from fMRI with uncorrected p -value < 0.001 . For the same corrected p -value ($0.01 \sim 0.1$), we can see that the sensitivity of OLS is larger than that of GLS with negligible loss of specificity.

Fig. 4.5 show the activation maps of HbO, HbR and HbT with using F statistic with LKC-based expected EC correction method. The contrast was chosen to see the effect of canonical hemodynamic response function (HRF). We can see that all the activation region are around primary motor cortex. Furthermore, compared to small activation map of HbR using t statistic, the activation are of HbR using F statistic is larger.

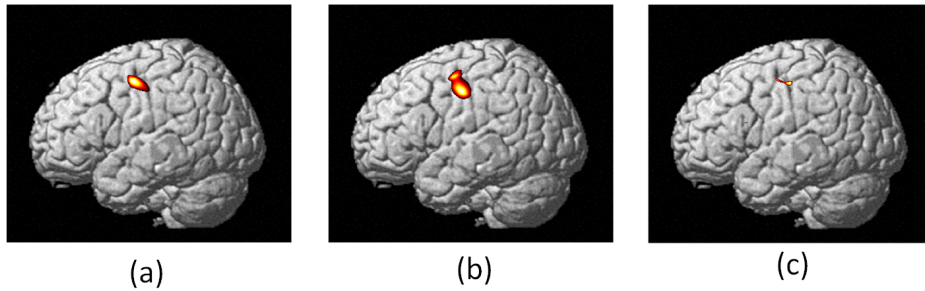


Figure 4.5: Group-level F maps using the LKC-based expected EC method: (a) activation map of HbO (corrected p -value < 0.05); (b) activation map of HbR (corrected p -value < 0.05); (c) activation map of HbT (corrected p -value < 0.05).

KAIST

Chapter 5. Discussion

In this paper, we found that the residual signals at each channel still have significant correlation, which is different from the standard assumption in mass-univariate approach in SPM. There may be several causes for this correlation. First, the design matrix is not sufficient to capture for all activation pattern, so the least-square residual signals may be a biased estimate of true noise components, so they still have synchronous signal components. To compensate for this, we may require more elaborate design matrix to capture all temporal dynamics, which is beyond the scope of this paper. Second, the global synchronous dynamics may exist in fNIRS due to vascular response. Recently, there are some reports saying that fNIRS signal contains global vascular response arising from the blood flow and oxidative metabolism [33, 34]. The fNIRS signals at different channels may be therefore highly correlated, which may lead to high correlation in least square residuals. Finally, since the spatial resolution of fNIRS is very low compared to fMRI, the neural activation tends to be blurring. Hence, the span of activation may appear across large area, which may make the channels correlated in terms of the least-square residual temporal dynamics. Note that in fMRI, even if there may exist spatial correlation between least square residuals, it is very difficult to include the effect in variance to estimate all t -value correction, since the number of voxels are extremely large and Σ_l in Eq. (2.11) is very difficult to store. Hence, the t -value correction proposed in this paper based on comparison between the tube formula and EC methods should be understood as unique feature for fNIRS.

KAIST

Chapter 6. Conclusion

This paper implements family-wise error rate using the LKC-based expected Euler characteristic for both individual- and group-level analyses. We showed that the result of individual t random field produced by Sun's tube formula coincides with that produced by LKC-based expected EC method by incorporating channel-wise least-square residual correlation. This provides a fNIRS unique t -value correction method by modifying mass-univariate assumption in fMRI. For the group-level t -test, both the generalized least square estimation and the ordinary least square estimation were studied and our results showed that the OLS approach was sensitive than the GLS case with negligible loss of specificity, and the reduced computational cost at individual analysis. We showed that the OLS-based group analysis is the choice that provides consistent multi-level analysis when precoloring is used at individual level. The results in this paper supplement the existing NIRS-SPM toolbox.



Appendix

Appendix A

The estimations of LCK for individual and group analyses are similar but still have some differences, so we give the estimation processes respectively.

Individual analysis

For a individual-level GLM, $\mathbf{y}_l(r) = \mathbf{X}\boldsymbol{\alpha}_l(r) + \boldsymbol{\epsilon}_l(r)$, the corresponding least-square residual is

$$\mathbf{r}_l(r) = \mathbf{y}_l(r) - \mathbf{X}\mathbf{X}^\dagger\mathbf{y}_l(r) = \mathbf{R}_{\mathbf{X}}\mathbf{y}_l(r),$$

and the corresponding normalized residual is

$$\mathbf{Q}_l(r) = \mathbf{r}_l(r)/\|\mathbf{r}_l(r)\| = \mathbf{R}_{\mathbf{X}}\mathbf{y}_l(r)/\|\mathbf{R}_{\mathbf{X}}\mathbf{y}_l(r)\|.$$

Let

$$\mathbf{S}_l(r) = \nabla\mathbf{Q}_l(r) = \begin{bmatrix} \frac{\partial\mathbf{Q}_l(r)}{\partial x} & \frac{\partial\mathbf{Q}_l(r)}{\partial y} \end{bmatrix},$$

where

$$\frac{\partial\mathbf{Q}_l(r)}{\partial x} = \frac{\partial\frac{\mathbf{R}_{\mathbf{X}}\mathbf{y}_l(r)}{\|\mathbf{R}_{\mathbf{X}}\mathbf{y}_l(r)\|}}{\partial x} = \frac{\mathbf{R}_{\mathbf{X}}\frac{\partial\mathbf{y}_l(r)}{\partial x}\|\mathbf{R}_{\mathbf{X}}\mathbf{y}_l(r)\| - \mathbf{R}_{\mathbf{X}}\mathbf{y}_l(r)\frac{\partial\|\mathbf{R}_{\mathbf{X}}\mathbf{y}_l(r)\|}{\partial x}}{\|\mathbf{R}_{\mathbf{X}}\mathbf{y}_l(r)\|^2}$$

and

$$\frac{\partial\mathbf{Q}_l(r)}{\partial y} = \frac{\partial\frac{\mathbf{R}_{\mathbf{X}}\mathbf{y}_l(r)}{\|\mathbf{R}_{\mathbf{X}}\mathbf{y}_l(r)\|}}{\partial y} = \frac{\mathbf{R}_{\mathbf{X}}\frac{\partial\mathbf{y}_l(r)}{\partial y}\|\mathbf{R}_{\mathbf{X}}\mathbf{y}_l(r)\| - \mathbf{R}_{\mathbf{X}}\mathbf{y}_l(r)\frac{\partial\|\mathbf{R}_{\mathbf{X}}\mathbf{y}_l(r)\|}{\partial y}}{\|\mathbf{R}_{\mathbf{X}}\mathbf{y}_l(r)\|^2}.$$

As shown in Appendix B, $\mathbf{y}_l(r) = (\mathbf{b}_l(r)^T \otimes \mathbf{I}_{\mathbf{N}}) \mathbf{y}_l$, so

$$\begin{aligned} \frac{\partial\mathbf{y}_l(r)}{\partial x} &= \frac{\partial((\mathbf{b}_l(r)^T \otimes \mathbf{I}_{\mathbf{N}}) \mathbf{y}_l)}{\partial x} = \left(\frac{\partial\mathbf{b}_l(r)^T}{\partial x} \otimes \mathbf{I}_{\mathbf{N}} \right) \mathbf{y}_l \\ \frac{\partial\mathbf{y}_l(r)}{\partial y} &= \frac{\partial((\mathbf{b}_l(r)^T \otimes \mathbf{I}_{\mathbf{N}}) \mathbf{y}_l)}{\partial y} = \left(\frac{\partial\mathbf{b}_l(r)^T}{\partial y} \otimes \mathbf{I}_{\mathbf{N}} \right) \mathbf{y}_l \end{aligned}$$

and

$$\begin{aligned} \frac{\partial\|\mathbf{R}_{\mathbf{X}}\mathbf{y}_l(r)\|}{\partial x} &= \frac{\frac{\partial\mathbf{y}_l^T(r)}{\partial x}\mathbf{R}_{\mathbf{X}}\mathbf{y}_l(r) + \mathbf{y}_l^T(r)\mathbf{R}_{\mathbf{X}}\frac{\partial\mathbf{y}_l(r)}{\partial x}}{2\|\mathbf{R}_{\mathbf{X}}\mathbf{y}_l(r)\|} \\ \frac{\partial\|\mathbf{R}_{\mathbf{X}}\mathbf{y}_l(r)\|}{\partial y} &= \frac{\frac{\partial\mathbf{y}_l^T(r)}{\partial y}\mathbf{R}_{\mathbf{X}}\mathbf{y}_l(r) + \mathbf{y}_l^T(r)\mathbf{R}_{\mathbf{X}}\frac{\partial\mathbf{y}_l(r)}{\partial y}}{2\|\mathbf{R}_{\mathbf{X}}\mathbf{y}_l(r)\|}. \end{aligned}$$

Since the basis function $\mathbf{b}_l(r)$ is given explicitly, the calculation of its derivatives can be done efficiently, so we can obtain the quantities for LKC-formula very easily.

Then, the estimation of 2-dimensional LKC of Φ_l is

$$\hat{\mathcal{L}}_2(\Phi_l) = \sum_{r \in \Phi_l} \det(\mathbf{S}_l(r)' \mathbf{S}_l(r))^{1/2},$$

which makes the largest contribution of the p -value approximation [23]. Since we have estimated $\hat{\mathcal{L}}_2(\Phi_l)$, assuming that the Φ_l is a disk, we can calculate $\hat{\mathcal{L}}_1(\Phi)$ and $\hat{\mathcal{L}}_0(\Phi)$ as follows [23]:

$$\hat{\mathcal{L}}_0(\Phi) = 1 \quad , \quad \hat{\mathcal{L}}_1(\Phi) = \pi r.$$

where $r = \sqrt{\hat{\mathcal{L}}_2(\Phi_l)/\pi}$.

Group analysis

Similar to the individual analysis, the first step is to estimate LKC. For $\hat{\alpha}(r) = \mathbf{X}_G \alpha_G(r) + \boldsymbol{\eta}'(r) \in \mathbb{R}^{ML}$, the corresponding least-square residual is

$$\mathbf{R}_G(r) = \hat{\alpha}(r) - \mathbf{X}_G \mathbf{X}_G^\dagger \hat{\alpha}(r).$$

and the corresponding normalized residual is

$$\mathbf{Q}_G(r) = \mathbf{R}_G(r) / \|\mathbf{R}_G(r)\|.$$

Let

$$\mathbf{S}_G(r) = (\mathbf{Q}_G(r + \delta_1) - \mathbf{Q}_G(r), \mathbf{Q}_G(r + \delta_2) - \mathbf{Q}_G(r)),$$

where δ_k is the 2-vector of zeros with k -th component equal to the lattice step size along axis k , $k = 1, 2$. For group analysis, the $\mathbf{S}_G(r)$ is difficult to be expressed as a close form, therefore a numerical method is used. Then, the estimation of 2-dimensional LKC of Φ_G is

$$\hat{\mathcal{L}}_{G_2}(\Phi_G) = \sum_{r \in \Phi_G} \det(\mathbf{S}_G(r)' \mathbf{S}_G(r))^{1/2},$$

which makes the largest contribution of the p -value approximation [23]. Since we have already estimated $\hat{\mathcal{L}}_{G_2}(\Phi_G)$, assuming that the Φ_G is a disk a short-cut for $\hat{\mathcal{L}}_{G_1}(\Phi_G)$ and $\hat{\mathcal{L}}_{G_0}(\Phi_G)$ is given by [23]:

$$\hat{\mathcal{L}}_{G_0}(\Phi_G) = 1 \quad , \quad \hat{\mathcal{L}}_{G_1}(\Phi_G) = \pi r.$$

where $r = \sqrt{\hat{\mathcal{L}}_{G_2}(\Phi_G)/\pi}$.

Appendix B

In [29], the individual-level GLM before interpolation is as follows:

$$\mathbf{y}_l = (\mathbf{I}_K \otimes \mathbf{X}) \boldsymbol{\beta}_l + \boldsymbol{\epsilon}_l,$$

where K denotes the number of channels, and $\boldsymbol{\beta}_l \in \mathbb{R}^{KM}$ are individual-level parameters for all channels. The interpolated time series at any position r can be derived as follows:

$$\begin{aligned} \mathbf{y}_l(r) &= (\mathbf{b}_l(r)^T \otimes \mathbf{I}_N) \mathbf{y}_l = (\mathbf{b}_l(r)^T \otimes \mathbf{I}_N) (\mathbf{I}_K \otimes \mathbf{X}) \boldsymbol{\beta}_l + \boldsymbol{\epsilon}_l(r) \\ &= (\mathbf{b}_l(r)^T \otimes \mathbf{X}) \boldsymbol{\beta}_l + \boldsymbol{\epsilon}_l(r) \\ &= (1 \otimes \mathbf{X}) (\mathbf{b}_l(r)^T \otimes \mathbf{I}_M) \boldsymbol{\beta}_l + \boldsymbol{\epsilon}_l(r) \\ &= \mathbf{X} (\mathbf{b}_l(r)^T \otimes \mathbf{I}_M) \boldsymbol{\beta}_l + \boldsymbol{\epsilon}_l(r) \\ &= \mathbf{X} \boldsymbol{\alpha}_l(r) + \boldsymbol{\epsilon}_l(r), \end{aligned}$$

where $\mathbf{b}_l(r)$ is the interpolated kernel and $\boldsymbol{\epsilon}_l(r) = (\mathbf{b}_l(r)^T \otimes \mathbf{I}_N) \boldsymbol{\epsilon}_l$. This implies that at any interpolated point, the same design matrix can be used for GLM.

Appendix C

The two-level model for the group analysis at the position r is given by

$$\mathbf{Y}(r) = \mathbf{D}\boldsymbol{\alpha}(r) + \boldsymbol{\epsilon}(r), \quad (\text{C.1})$$

$$\boldsymbol{\alpha}(r) = \mathbf{X}_{\mathbf{G}}\boldsymbol{\alpha}_{\mathbf{G}}(r) + \boldsymbol{\eta}(r), \quad (\text{C.2})$$

where

$$\mathbf{X}_{\mathbf{G}} = \mathbf{1}_L \otimes \mathbf{I}_M = \begin{bmatrix} 1 & 1 & \cdots & 1 \end{bmatrix}^T \otimes \mathbf{I}_M \in \mathbb{R}^{ML \times M}$$

is group-level design matrix, $\boldsymbol{\alpha}_{\mathbf{G}}(r) \in \mathbb{R}^M$ is group-level signal responses or parameters, $\boldsymbol{\eta}(r) \in \mathbb{R}^{ML}$ denotes the between-subject variance, respectively. Substituting Eq. (C.2) into Eq. (C.1), we can obtain the single-level model for group analysis:

$$\begin{aligned} \mathbf{Y}(r) &= \mathbf{D}(\mathbf{X}_{\mathbf{G}}\boldsymbol{\alpha}_{\mathbf{G}}(r) + \boldsymbol{\eta}(r)) + \boldsymbol{\epsilon}(r) \\ &= \mathbf{D}\mathbf{X}_{\mathbf{G}}\boldsymbol{\alpha}_{\mathbf{G}}(r) + \boldsymbol{\gamma}(r), \end{aligned} \quad (\text{C.3})$$

where $\boldsymbol{\gamma}(r) = \mathbf{D}\boldsymbol{\eta}(r) + \boldsymbol{\epsilon}(r) \in \mathbb{R}^{NL}$ and the covariance is given by

$$\mathbf{C}_{\boldsymbol{\gamma}} = \mathbf{D}\mathbf{C}_{\boldsymbol{\eta}}\mathbf{D}^T + \mathbf{C}_{\boldsymbol{\epsilon}} \in \mathbb{R}^{NL \times NL}. \quad (\text{C.4})$$

In ‘‘summary statistics’’ approach, second-level model uses the estimates of first-level parameters $\hat{\boldsymbol{\alpha}}(r)$. Specifically, ‘‘summary statistics’’ model for group analysis is as follows:

$$\mathbf{Y}(r) = \mathbf{D}\hat{\boldsymbol{\alpha}}(r) + \boldsymbol{\epsilon}(r), \quad (\text{C.5})$$

$$\hat{\boldsymbol{\alpha}}(r) = \mathbf{X}_{\mathbf{G}}\boldsymbol{\alpha}_{\mathbf{G}}(r) + \boldsymbol{\eta}'(r) \in \mathbb{R}^{ML} \quad (\text{C.6})$$

where $\boldsymbol{\eta}'(r)$ is the equivalent residual error term.

OLS-based t -test

First, applying the ordinary least square to the single-level group analysis Eq. (C.3), the group-level parameter estimate $\hat{\boldsymbol{\alpha}}_{\mathbf{G}}(r)$ is given by

$$\hat{\boldsymbol{\alpha}}_{\mathbf{G}}(r) = (\mathbf{D}\mathbf{X}_{\mathbf{G}})^{\dagger} \mathbf{Y}(r) \in \mathbb{R}^M, \quad (\text{C.7})$$

and its error covariance is

$$\mathbf{C}_{\hat{\boldsymbol{\alpha}}_{\mathbf{G}}(r)} = (\mathbf{D}\mathbf{X}_{\mathbf{G}})^{\dagger} \mathbf{C}_{\boldsymbol{\gamma}} (\mathbf{D}\mathbf{X}_{\mathbf{G}})^{\dagger T} \in \mathbb{R}^{M \times M}. \quad (\text{C.8})$$

Now, for the ‘‘summary statistics’’ group analysis, the ordinary least square method gives the estimates and its covariance for the first-level Eq. (C.5):

$$\hat{\boldsymbol{\alpha}}(r) = \mathbf{D}^{\dagger} \mathbf{Y}(r), \quad (\text{C.9})$$

$$\mathbf{C}_{\hat{\boldsymbol{\alpha}}(r)} = \mathbf{D}^{\dagger} \mathbf{C}_{\boldsymbol{\epsilon}} \mathbf{D}^{\dagger T} \in \mathbb{R}^{ML \times ML}. \quad (\text{C.10})$$

We also apply the ordinary least-square estimation to Eq. (C.6), which provides us the group-level parameter estimate of the ‘‘summary statistics’’ approach:

$$\hat{\boldsymbol{\alpha}}_{\mathbf{G}}(r) = \mathbf{X}_{\mathbf{G}}^{\dagger} \hat{\boldsymbol{\alpha}}(r) \quad (\text{C.11})$$

$$= \mathbf{X}_{\mathbf{G}}^{\dagger} \mathbf{D}^{\dagger} \mathbf{Y}(r) \in \mathbb{R}^M \quad (\text{C.12})$$

where we use Eq. (C.9). The resulting error covariance is then given by

$$\mathbf{C}_{\hat{\alpha}_{\mathbf{G}}(r)} = \mathbf{X}_{\mathbf{G}}^{\dagger} \mathbf{C}_{\eta'} \mathbf{X}_{\mathbf{G}}^{\dagger T} \in \mathbb{R}^{M \times M}. \quad (\text{C.13})$$

In order to make “summary statistics” approach equivalent to the single-level group analysis, we should make Eqs. (C.7) (C.8) equal to Eqs. (C.12) (C.13), respectively. Since $(\mathbf{D}\mathbf{X}_{\mathbf{G}})^{\dagger} = \mathbf{X}_{\mathbf{G}}^{\dagger} \mathbf{D}^{\dagger}$ as shown in Appendix D, it is easy to check that Eq. (C.7) is equal to Eq. (C.12). Furthermore, since Eq. (C.8) can be rewritten as

$$\mathbf{C}_{\hat{\alpha}_{\mathbf{G}}(r)} = \mathbf{X}_{\mathbf{G}}^{\dagger} \mathbf{D}^{\dagger} \mathbf{C}_{\gamma} \mathbf{D}^{\dagger T} \mathbf{X}_{\mathbf{G}}^{\dagger T}, \quad (\text{C.14})$$

the condition for the equivalence of Eq. (C.13) and Eq. (C.8) can be satisfied if and only if

$$\mathbf{C}_{\eta'} = \mathbf{D}^{\dagger} \mathbf{C}_{\gamma} \mathbf{D}^{\dagger T}. \quad (\text{C.15})$$

Substituting Eq. (C.4) into Eq. (C.15):

$$\begin{aligned} \mathbf{C}_{\eta'} &= \mathbf{D}^{\dagger} (\mathbf{D} \mathbf{C}_{\eta} \mathbf{D}^T) \mathbf{D}^{\dagger T} + \mathbf{D}^{\dagger} \mathbf{C}_{\epsilon} \mathbf{D}^{\dagger T} \\ &= \mathbf{C}_{\eta} + \mathbf{D}^{\dagger} \mathbf{C}_{\epsilon} \mathbf{D}^{\dagger T} \\ &= \mathbf{C}_{\eta} + \mathbf{C}_{\hat{\alpha}(r)}, \end{aligned} \quad (\text{C.16})$$

since $\mathbf{D}^{\dagger} \mathbf{D} = \mathbf{I}_{L(r)}$ and $\mathbf{D}^T \mathbf{D}^{\dagger T} = \mathbf{I}_L$.

Therefore, the “summary statistics” model for group analysis is given by Eq. (C.5) and Eq. (C.6) if we assume that the noise variance for $\mathbf{C}_{\eta'}$ is given by

$$\mathbf{C}_{\eta'} = \mathbf{C}_{\eta} + \mathbf{C}_{\hat{\alpha}(r)} \quad (\text{C.17})$$

$$= \mathbf{C}_{\eta} + \begin{bmatrix} \mathbf{C}_{\hat{\alpha}_1(r)} & \mathbf{O} & \cdots & \mathbf{O} \\ \mathbf{O} & \mathbf{C}_{\hat{\alpha}_2(r)} & \cdots & \mathbf{O} \\ \vdots & \vdots & \ddots & \vdots \\ \mathbf{O} & \mathbf{O} & \cdots & \mathbf{C}_{\hat{\alpha}_L(r)} \end{bmatrix} \in \mathbb{R}^{ML \times ML}, \quad (\text{C.18})$$

Note that the adjusted second-level covariance matrix Eq. (C.18) is represented as the sum of the within- and between-subject covariances [2].

Since the group estimate $\hat{\alpha}_{\mathbf{G}}(r)$ and its error covariance are given by

$$\hat{\alpha}_{\mathbf{G}}(r) = \mathbf{X}_{\mathbf{G}}^{\dagger} \hat{\alpha}(r), \quad (\text{C.19})$$

$$\mathbf{C}_{\hat{\alpha}_{\mathbf{G}}(r)} = \mathbf{X}_{\mathbf{G}}^{\dagger} \mathbf{C}_{\eta'} \mathbf{X}_{\mathbf{G}}^{\dagger T}, \quad (\text{C.20})$$

using $\mathbf{C}_{\eta} = \mathbf{I}_L \otimes \sigma_s^2 \mathbf{I}_M$, we have the following simple forms:

$$\begin{aligned} \hat{\alpha}_{\mathbf{G}}(r) &= \mathbf{X}_{\mathbf{G}}^{\dagger} \hat{\alpha}(r) \\ &= \frac{1}{L} \sum_{l=1}^L \hat{\alpha}_l(r), \end{aligned} \quad (\text{C.21})$$

$$\begin{aligned} \mathbf{C}_{\hat{\alpha}_{\mathbf{G}}(r)} &= \mathbf{X}_{\mathbf{G}}^{\dagger} \mathbf{C}_{\eta'} \mathbf{X}_{\mathbf{G}}^{\dagger T} \\ &= \frac{1}{L^2} \sum_{l=1}^L (\sigma_s^2 \mathbf{I}_M + \mathbf{C}_{\hat{\alpha}_l(r)}). \end{aligned} \quad (\text{C.22})$$

Then, a response at a particular condition as an inner product with a contrast vector is given by

$$\begin{aligned}\hat{\boldsymbol{\chi}}_{\mathbf{G}}(r) &= \mathbf{c}^T \hat{\boldsymbol{\alpha}}_{\mathbf{G}}(r) \\ &= \frac{1}{L} \sum_{l=1}^L \hat{\boldsymbol{\chi}}_l(r),\end{aligned}\tag{C.23}$$

$$= \mathbf{1}_L^\dagger \hat{\boldsymbol{\chi}}(r),\tag{C.24}$$

where $\hat{\boldsymbol{\chi}}_l(r)$ is the contrast of estimated individual-level parameter and $\hat{\boldsymbol{\chi}}(r) = [\hat{\boldsymbol{\chi}}_1(r) \cdots \hat{\boldsymbol{\chi}}_L(r)]^T$. The corresponding covariance is

$$\begin{aligned}\mathbf{C}_{\hat{\boldsymbol{\chi}}_{\mathbf{G}}(r)} &= \mathbf{c}^T \mathbf{C}_{\hat{\boldsymbol{\alpha}}_{\mathbf{G}}(r)} \mathbf{c} \\ &= \frac{1}{L^2} \sum_{l=1}^L (\mathbf{c}^T (\sigma_s^2 \mathbf{I}_{\mathbf{M}} + \mathbf{C}_{\hat{\boldsymbol{\alpha}}_l(r)}) \mathbf{c}) \\ &= \frac{1}{L^2} \sum_{l=1}^L (\sigma_s^2 \mathbf{c}^T \mathbf{c} + C_{\hat{\boldsymbol{\chi}}_l(r)})\end{aligned}\tag{C.25}$$

$$= \mathbf{1}_L^\dagger \mathbf{C}_{\boldsymbol{\omega}} \mathbf{1}_L^T,\tag{C.26}$$

and

$$\mathbf{C}_{\boldsymbol{\omega}} = \mathbf{C}_{\hat{\boldsymbol{\chi}}(r)} + \sigma_s^2(r) \mathbf{c}^T \mathbf{c} \mathbf{I} = \begin{bmatrix} C_{\hat{\boldsymbol{\chi}}_1(r)} & \mathbf{0} & \cdots & \mathbf{0} \\ \mathbf{0} & C_{\hat{\boldsymbol{\chi}}_2(r)} & \cdots & \mathbf{0} \\ \vdots & \vdots & \ddots & \vdots \\ \mathbf{0} & \mathbf{0} & \cdots & C_{\hat{\boldsymbol{\chi}}_L(r)} \end{bmatrix} + \sigma_s^2(r) \mathbf{c}^T \mathbf{c} \mathbf{I}.\tag{C.27}$$

For the ordinary least square approach, a group-level t -statistic for detecting significance can be performed by

$$T_G(r) = \frac{\hat{\boldsymbol{\chi}}_{\mathbf{G}}(r)}{\sqrt{C_{\hat{\boldsymbol{\chi}}_{\mathbf{G}}(r)}}}\tag{C.28}$$

$$= \frac{\sum_{l=1}^L \hat{\boldsymbol{\chi}}_l(r)}{\sqrt{\sum_{l=1}^L (\sigma_s^2 \mathbf{c}^T \mathbf{c} + C_{\hat{\boldsymbol{\chi}}_l(r)})}}.\tag{C.29}$$

It has been shown that algebraic sum of individual random fields in Eq. (C.29) has the degree of freedom given by [17, 26]

$$df_G = \frac{\sum_{l=1}^L (\sigma_s^2 \mathbf{c}^T \mathbf{c} + C_{\hat{\boldsymbol{\chi}}_l(r)})^2}{\frac{L\sigma_s^4 (\mathbf{c}^T \mathbf{c})^2}{L-1} + \sum_{l=1}^L \frac{C_{\hat{\boldsymbol{\chi}}_l(r)}^2}{df_l}},\tag{C.30}$$

where df_l is the degree of freedom for $\hat{\boldsymbol{\chi}}_l(r)$.

Appendix D

Our goal is to prove $(\mathbf{D}\mathbf{X}_{\mathbf{G}})^\dagger = \mathbf{X}_{\mathbf{G}}^\dagger \mathbf{D}^\dagger$. Note that

$$\begin{aligned}(\mathbf{D}\mathbf{X}_{\mathbf{G}})^\dagger &= ((\mathbf{I}_{L(r)} \otimes \mathbf{X})\mathbf{X}_{\mathbf{G}})^\dagger \\ &= ((\mathbf{I}_{L(r)} \otimes \mathbf{X})(\mathbf{1}_{L(r)} \otimes \mathbf{I}_{\mathbf{M}}))^\dagger \\ &= (\mathbf{1}_{L(r)} \otimes \mathbf{X})^\dagger \\ &= \frac{1}{L(r)} (\mathbf{1}_{L(r)}^T \otimes \mathbf{X}^\dagger).\end{aligned}$$

Second, the right side of the equation is given by:

$$\begin{aligned}\mathbf{X}_G^\dagger &= \frac{1}{L(r)}(\mathbf{1}_{L(r)}^T \otimes \mathbf{I}_M) \\ \mathbf{D}^\dagger &= (\mathbf{I}_{L(r)} \otimes \mathbf{X})^\dagger = \mathbf{I}_{L(r)} \otimes \mathbf{X}^\dagger \\ \mathbf{X}_G^\dagger \mathbf{D}^\dagger &= \frac{1}{L(r)}(\mathbf{1}_{L(r)}^T \otimes \mathbf{I}_M) (\mathbf{I}_{L(r)} \otimes \mathbf{X}^\dagger) \\ &= \frac{1}{L(r)}(\mathbf{1}_{L(r)}^T \otimes \mathbf{X}^\dagger).\end{aligned}$$

Since both sides are equal, this concludes the proof.

The logo for KAIST (Korea Advanced Institute of Science and Technology) is centered at the bottom of the page. It consists of the letters "KAIST" in a bold, blue, sans-serif font, with a light blue horizontal oval shape underneath it.

References

- [1] Adler, R., Taylor, J., Random fields and geometry, Springer Verlag, 2007.
- [2] Beckmann, C., Jenkinson, M., Smith, S., “General multilevel linear modeling for group analysis in fMRI,” *Neuroimage* 20 (2), 1052.1063 (2003).
- [3] Bianciardi, M., Cerasa, A., Patria, F., Hagberg, G., “Evaluation of mixed effects in event-related fmri studies: impact of first-level design and filtering,” *Neuroimage* 22 (3), 1351.1370 (2004).
- [4] Boas, D., Gaudette, T., Strangman, G., Cheng, X., Marota, J., Mandeville, J., “The accuracy of near infrared spectroscopy and imaging during focal changes in cerebral hemodynamics,” *Neuroimage* 13 (1), 76.90 (2001).
- [5] Boas, D., Strangman, G., Culver, J., Hoge, R., Jaszewski, G., Poldrack, R., Rosen, B., Mandeville, J., “Can the cerebral metabolic rate of oxygen be estimated with near-infrared spectroscopy?,” *Physics in medicine and biology* 48, 2405 (2003).
- [6] Cnaan, A., Laird, N., Slasor, P., “Tutorial in biostatistics: using the general linear mixed model to analyse unbalanced repeated measures and longitudinal data,” *Statistics in Medicine* 16, 2349.2380 (1997).
- [7] Cope, M., Delpy, D., “System for long-term measurement of cerebral blood and tissue oxygenation on newborn infants by near infra-red transillumination,” *Medical and Biological Engineering and Computing* 26 (3), 289.294 (1988).
- [8] Friston, K., Ashburner, J., Kiebel, S., Nichols, T., Penny, W. (Eds.), “Statistical Parametric Mapping: The Analysis of Functional Brain Images,” Academic Press, 2007.
- [9] Hess, A., Stiller, D., Kaulisch, T., Heil, P., Scheich, H., “New insights into the hemodynamic blood oxygenation level-dependent response through combination of functional magnetic resonance imaging and optical recording in gerbil barrel cortex,” *The Journal of Neuroscience* 20 (9), 3328 (2000).
- [10] Jang, K., Tak, S., Jung, J., Jang, J., Jeong, Y., Ye, J., “Wavelet minimum description length detrending for near-infrared spectroscopy,” *Journal of Biomedical Optics* 14, 034004 (2009).
- [11] Kleinschmidt, A., Obrig, H., Requardt, M., Merboldt, K., Dirnagl, U., Villringer, A., Frahm, J., “Simultaneous recording of cerebral blood oxygenation changes during human brain activation by magnetic resonance imaging and near-infrared spectroscopy,” *Journal of Cerebral Blood Flow and Metabolism* 16 (5), 817.826 (1996).
- [12] Koh, P., Glaser, D., Flandin, G., Kiebel, S., Butterworth, B., Maki, A., Delpy, D., Elwell, C., “Functional optical signal analysis: a software tool for near-infrared spectroscopy data processing incorporating statistical parametric mapping,” *Journal of Biomedical Optics* 12, 064010 (2007).
- [13] Matthews, J., Altman, D., Campbell, M., Royston, P., “Analysis of serial measurements in medical research,” *British Medical Journal* 300 (6719), 230 (1990).

- [14] Mehagnoul-Schipper, D., van der Kallen, B., Colier, W., van der Sluijs, M., van Erning, L., Thijssen, H., Oeseburg, B., Hoefnagels, W., Jansen, R., “Simultaneous measurements of cerebral oxygenation changes during brain activation by near-infrared spectroscopy and functional magnetic resonance imaging in healthy young and elderly subjects,” *Human brain mapping* 16 (1), 14.23 (2002).
- [15] Okamoto, M., Dan, H., Shimizu, K., Takeo, K., Amita, T., Oda, I., Konishi, I., Sakamoto, K., Isobe, S., Suzuki, T., et al., “Multimodal assessment of cortical activation during apple peeling by nirs and fmri,” *Neuroimage* 21 (4), 1275.1288 (2004).
- [16] Plichta, M., Heinzl, S., Ehlis, A., Pauli, P., Fallgatter, A., “Model-based analysis of rapid event-related functional near-infrared spectroscopy (NIRS) data: A parametric validation study,” *Neuroimage* 35 (2), 625.634 (2007).
- [17] Satterthwaite, F., “An approximate distribution of estimates of variance components,” *Biometrics Bulletin* 2 (6), 110.114 (1946).
- [18] Schroeter, M.L. and Bucheler, M.M. and Muller, K. and Uluda, K. and Obrig, H. and Lohmann, G. and Tittgemeyer, M. and Villringer, A. and Von Cramon, D.Y., “Towards a standard analysis for functional near-infrared imaging,” *NeuroImage* 21 (1), 283.290 (2004).
- [19] Strangman, G., Culver, J., Thompson, J., Boas, D., “A quantitative comparison of simultaneous BOLD fMRI and NIRS recordings during functional brain activation,” *NeuroImage* 17 (2), 719.731 (2002).
- [20] Takemura, A., Kuriki, S., “Maximum of gaussian field on piecewise smooth domain: Equivalence of tube method and euler characteristic method,” *Ann. Appl. Probab* 12, 768.796 (2002).
- [21] Takemura, A., Kuriki, S., “Tail probability via the tube formula when the critical radius is zero,” *Bernoulli* 9 (3), 535.558 (2003).
- [22] Taylor, J., Worsley, K., “Detecting sparse signals in random fields, with an application to brain mapping,” *Journal of the American Statistical Association* 102 (479), 913.928 (2007).
- [23] Taylor, J., Worsley, K., “Random fields of multivariate test statistics, with applications to shape analysis,” *Annals of Statistics* 36 (1), 1.27 (2008).
- [24] Toronov, V., Webb, A., Choi, J., Wolf, M., Michalos, A., Gratton, E., Hueber, D., “Investigation of human brain hemodynamics by simultaneous near-infrared spectroscopy and functional magnetic resonance imaging,” *Medical Physics* 28, 521 (2001).
- [25] Villringer, A., Dirnagl, U., “Coupling of brain activity and cerebral blood flow: basis of functional neuroimaging,” *Cerebrovascular and brain metabolism reviews* 7 (3), 240 (1995).
- [26] Welch, B., “The generalization of student’s problem when several different population variances are involved,” *Biometrika* 34 (1/2), 28.35 (1947).
- [27] Worsley, K., Andermann, M., Koulis, T., MacDonald, D., Evans, A., “Detecting changes in non-isotropic images,” *Human Brain Mapping* 8 (2-3), 98.101 (1999).
- [28] Ye, J., Moulin, P., Bresler, Y., “Asymptotic global confidence regions for 3-d parametric shape estimation in inverse problems,” *Image Processing, IEEE Transactions on* 15 (10), 2904.2919 (2006).

- [29] Ye, J., Tak, S., Jang, K., Jung, J., Jang, J., “NIRS-SPM: statistical parametric mapping for near-infrared spectroscopy,” *Neuroimage* 44 (2), 428-447 (2009).
- [30] M. L., Bucheler, M. M., Muller, K., Uludag, K., Obrig, H., Lohmann, G., Tittgemeyer, M., Villringer, A., von Cramon, D. Y., “Towards a standard analysis for functional near-infrared imaging,” *Neuroimage* 21, 283-290 (2004).
- [31] Worsley, K., “Boundary corrections for the expected Euler characteristic of excursion sets of random fields, with an application to astrophysics,” *Advances in Applied Probability* 27 (4), 943-959 (1999).
- [32] Monti, M., “Statistical analysis of fMRI time-series: a critical review of the GLM approach,” *Frontiers in Human Neuroscience* 5 (2011).
- [33] Tong, Y., et al., “Time lag dependent multimodal processing of concurrent fMRI and near-infrared spectroscopy (NIRS) data suggests a global circulatory origin for low-frequency oscillation signals in human brain,” *Neuroimage* 53 (2), 553-564 (2010).
- [34] Gagnon, L., Perdue, K., Greve, D., Goldenholz, D., Kaskhedikar, G., Boas, D., “Improved recovery of the hemodynamic response in diffuse optical imaging using short optode separations and state-space modeling,” *Neuroimage* (2011).

